

Tidal Energy Loss, Internal Tide Radiation, and Local Dissipation for Two-Layer Tidal Flow over a Sill

LARS ARNEBORG

Department of Marine Sciences, University of Gothenburg, Gothenburg, and Department of Research and Development, Swedish Meteorological and Hydrological Institute, Norrköping, Sweden

PÄR JANSSON

Centre for Arctic Gas Hydrate, Environment and Climate, and Department of Geology, University of Tromsø—The Arctic University of Norway, Tromsø, Norway

ANDRÉ STAALSTRØM

Section for Biogeochemistry and Physical Oceanography, Norwegian Institute for Water Research, Oslo, Norway

GÖRAN BROSTRÖM

Department of Marine Sciences, University of Gothenburg, Gothenburg, Sweden

(Manuscript received 23 June 2016, in final form 17 March 2017)

ABSTRACT


A simple analytical model for tidal energy loss at fjord sills and its partitioning into local dissipation and radiated internal tides is presented. The analytical model builds on a two-layer assumption with quasi-steady nonlinear flow over the sill and wave radiation in the far field. When the interface is situated above sill level, upstream- and downstream-propagating internal waves are generated as the bottom-layer flow becomes partially blocked because of a hydraulic control over the sill. When this control sets in, energy is lost in the transition from supercritical flow over the sill to subcritical flow downstream of the sill. The analytical model is compared with observations at the Drøbak sill in the Oslo Fjord and with idealized numerical simulations with a nonhydrostatic primitive equation model. The overall good agreement between observations, analytical model, and numerical model results indicates that the hydraulic control over the sill is a key player for both the generation of internal tides and the local energy loss. The tidal energy loss decreases with increasing height of the interface above the sill. At the same time, the fraction of energy dissipated locally increases from about 20% for the interface situated at sill level to >50% when the upper-layer thickness is less than about 80% of the sill depth. These results correspond well with the observations in the Oslo Fjord where more energy is dissipated near the sill than is radiated away.

1. Introduction

The oscillating flow of stratified fluids over topography has received much attention since it was recognized that tides lose considerable amounts of energy at rough topography in the deep ocean (Sjöberg and

Stigebrandt 1992; Egbert and Ray 2000) and that this may explain a large part of the energy required to mix the abyssal ocean (Munk and Wunsch 1998). It has also received attention because tidal flow over fjord sills seems to be related to the strength of mixing in fjord basins and thereby governs the ventilation and the amount of oxygen-consuming material a fjord can receive without developing oxygen deficiency (e.g., Stigebrandt et al. 1996).

The small dimensions of fjords relative to the deep ocean, their sill at the entrance, and the often relatively strong currents over the sill that are needed to adjust the

 Denotes content that is immediately available upon publication as open access.

Corresponding author: Lars Arneborg, lars.arneborg@smhi.se

fjord state to the variable conditions outside the fjord make them excellent places to study stratified flow over topography. The fjord studies have mainly followed two branches. One branch (e.g., Stigebrandt 1976, 1979; Stigebrandt and Aure 1989; Stacey 1985) has focused on the harmonic forcing of internal tides of the same frequency as the tidal forcing. Stigebrandt and Aure (1989) showed that the amount of work needed to mix the basin waters inside fjord sills was proportional to theoretical estimates of the energy flow into internal tides radiating away from the sills. The suggested dissipation mechanism was the breaking of internal tides at the sloping topography away from the sill. Some peculiarities of that theory is that the relation seems to hold even for fjords much shorter than the internal waves claimed to cause the mixing and that it assumes that the internal tides mainly lose their energy below sill level. To our knowledge, internal tide wave breaking away from the sill of fjords remains to be confirmed. Another branch (e.g., Farmer and Armi 1999; Klymak and Gregg 2004; Inall et al. 2004; Staalstrøm et al. 2015) has focused on the internal hydraulics at fjord sills, where tidal flow often causes large internal hydraulic jumps on the lee side of sills. We have found no fjord studies systematically investigating the relative amounts of tidal energy going into hydraulic jumps and radiated internal tides and the importance of these components for basin water mixing. However, there are a number of recent studies in ocean settings investigating these questions (see below).

Based on a dataset from Oslo Fjord in June 2012, Staalstrøm et al. (2015, hereinafter SALB) showed that most of the tidal energy loss dissipated close to the sill in strong hydraulic jumps and that only about 10%–40% of the barotropic energy loss radiated into the fjord as internal tide energy. This is a similar fraction of radiated to dissipated energy, as in the much more energetic Loch Etive (Inall et al. 2004; Stashchuk et al. 2007), and much smaller than in Knight Inlet, where as much as two-thirds radiates into the fjord (Klymak and Gregg 2004). The most ambitious campaign to measure radiated and dissipated energy losses at a topographic ridge has been done in Hawaii in the Hawaiian Ocean Mixing Experiment (HOME) experiment, where 15% of the total barotropic energy loss was estimated to dissipate locally near the topography (Klymak et al. 2006). In some ocean general circulation models (OGCMs) tidal mixing has since then been parameterized under the assumption that 1/3 of the barotropic tidal energy loss dissipates locally and contributes to mixing, whereas the radiated part is unaccounted for (e.g., Simmons et al. 2004; Saenko and

Merryfield 2005). Examples of later estimates of the fraction of tidal loss dissipated locally, based mainly on high-resolution numerical models, Musgrave et al. (2016; Mendocino Escarpment, 28%), and Alford et al. (2015; Luzon Strait, 40%), indicate that the fraction is variable but do not provide any direct answers to the reason for this variability.

A serious attempt to understand the fraction of energy dissipated locally was done in a model study (Klymak et al. 2010) that suggested that the total barotropic energy loss was well described by linear internal wave generation theory and that the dissipated part corresponds to the energy flux contribution from the high modes that have a group velocity that is too small to escape the topography. This model predicts a much smaller local dissipation at the Hawaii Ridge than the 15% estimated from the HOME observations. In addition, it predicts a dissipation that increases with the tidal velocity amplitude cubed, whereas the results in Musgrave et al. (2016) suggest something closer to the tidal velocity squared. Winters and Armi (2012, 2013) discussed the dynamics of continuously stratified, blocked tidal flow over a sill and nicely showed that for most supercritical crests a quasi-steady, hydraulic-controlled flow develops in a layer above the crest and that this reduces the generation of radiated internal tides. However, they did not present a theory to predict this reduction in internal tides or the energy dissipated in the nonlinear flow near the sill.

In the present paper, we investigate the relationship between local energy loss at the sill and internal tide radiation and reuse and develop a set of existing theories to predict energy flux in the internal tide and local dissipation in a hydraulic jump for the idealized two-layer tidal flow over a short, steep sill. The theoretical development basically builds on the development of Baines (1988) and subsequent papers but is applied in a quasi-steady sense on an oscillating tidal flow to obtain the abovementioned energy partitioning. There is considerable literature on two-layer jumps and bores and on the ability of two-layer hydraulic theory to predict energy losses in jumps (e.g., Chu and Baddour 1977; Wood and Simpson 1984; Baines 1984; Klemp et al. 1997; Li and Cummins 1998; White and Helfrich 2014). In the present work, these propagating bores belong to the radiated part of the energy that is extracted from the barotropic tides, and their energy losses are therefore not considered. Inspired by observations (e.g., SALB), the local energy loss at the sill is assumed to be caused by a quasi-steady hydraulic jump at the sill, a feature that has received much less theoretical attention (e.g., Holland

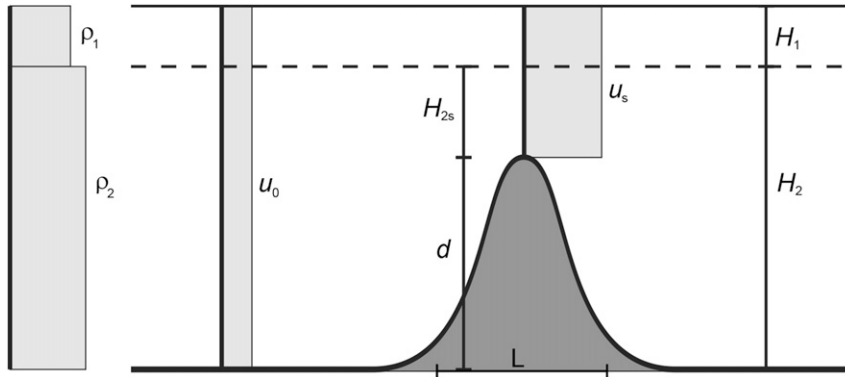


FIG. 1. Definition sketch of two-layer flow over a sill, showing the barotropic velocities u_0 and u_s away from and over the sill, respectively.

et al. 2002) than the two-layer bore moving into stationary water. The energy loss in that jump is mainly governed by the differences in energy heads upstream and downstream of the sill, which in turn are governed by the blocking at the sill in the case the flow is hydraulically controlled there. Entrainment into the jump is assumed to be of secondary importance relative to the downstream baroclinic volume flux changes imposed by the sill and the hydraulic control. Under these assumptions, it turns out that it suffices to describe the hydraulic control at the sill and the upstream and downstream propagation of internal waves to predict both the local energy loss and the radiated energy, as described in more detail below. The theoretical two-layer predictions are compared with the 2012 Oslo Fjord dataset also presented in SALB and with two-dimensional, high-resolution simulations with the nonhydrostatic MITgcm model over idealized topography.

In section 2, we present the theory and the method used to calculate energy fluxes in the theory and in the numerical simulations. In section 3, we briefly present the dataset from the Oslo Fjord. In section 4, we describe the idealized numerical simulations, and in section 5, we compare the theoretical predictions with the observations and the results of the numerical simulations. The results are discussed in section 6.

2. Theory

We consider a time-varying, uniform-width, two-layer barotropic flow over a sill (Fig. 1) with the deep-water barotropic velocity u_0 varying in time as

$$u_0 = U_0 \cos(\omega t), \quad (1)$$

where U_0 is the barotropic velocity amplitude, and ω is the tidal frequency. Assuming a much smaller surface elevation than interface changes (rigid-lid

approximation), the barotropic volume flux can be considered independent of position x , which means that the barotropic velocity at the sill u_s is related to that in deep water as

$$u_s = \frac{H}{H-d} u_0, \quad (2)$$

where H is the deep-water depth, and d is the height of the sill. Now, we combine two approximations to describe the time-varying hydraulic flow over the sill and the internal wave radiation away from the sill. In the near field over the sill, we assume that the flow quickly adjusts to a quasi-steady state in equilibrium with the barotropic forcing at that time. In order for that to be true, the tidal excursion length (e.g., Winters and Armi 2013) must be large relative to the width of the sill L during a tidal cycle. This can be expressed as

$$\frac{U_s}{\omega L} \gg 1, \quad (3)$$

where U_s is the barotropic velocity amplitude over the sill. This may be a conservative estimate since the lower-layer velocity is larger than the barotropic sill velocity; furthermore, the lower layer may only be hydraulically active in a region close to the sill crest. The resulting two-layer hydraulic flow over a sill is thoroughly described in Baines (1995), which we to some extent follow here. In the far field away from the sill, the sill is mainly felt by the restrictions in volume fluxes in the upper and lower layers, imposed by the near-field hydraulics at the sill. These cause internal waves to be radiated away from the sill, raising the interface on the upstream side and lowering it on the downstream side. A further assumption here is that the mixing at the sill does not have a strong impact on the layer volume fluxes. The local energy loss is

then calculated from the change in lower-layer Bernoulli function, assuming that no energy loss takes place in the upper layer, as described further below. A somewhat provocative implication of these assumptions is that the integrated local energy loss is determined by the large-scale flow via the hydraulic control and the internal wave radiation rather than by small-scale processes, such as shear instability, internal wave overturning, and so on.

a. Near-field flow

In the hydraulic theory, we assume that volume fluxes are conserved in each layer, that no mixing occurs between the layers, and that (apart from in the hydraulic jumps) energy is conserved in each layer. The volume flux in each layer can be written as the barotropic part plus the baroclinic part, that is,

$$q_1 = u_0 H_1 + q_{bc}, \quad \text{and} \quad (4)$$

$$q_2 = u_0 H_2 - q_{bc}, \quad (5)$$

where q_{bc} is the baroclinic part of the volume flux counted positive in the upper layer and negative in the lower layer. These are of equal magnitude due to the rigid-lid assumption. Given the volume conservation in each layer, the upper- and lower-layer velocities at the sill, u_{1s} and u_{2s} , and upstream, u_{1u} and u_{2u} , can be calculated as

$$u_{1s} = \frac{q_1}{H_1 - \eta_s}, \quad u_{1u} = \frac{q_1}{H_1 - \eta_u}, \quad \text{and} \quad (6)$$

$$u_{2s} = \frac{q_2}{H_2 - d + \eta_s}, \quad u_{2u} = \frac{q_2}{H_2 + \eta_u}, \quad (7)$$

where η_u (η_s) is the interface elevation upstream (at the sill).

Energy conservation in both layers can, using the Boussinesq and hydrostatic approximations, be expressed as (e.g., Baines 1995)

$$\frac{1}{2}(u_{2u}^2 - u_{1u}^2) + g' \eta_u = \frac{1}{2}(u_{2s}^2 - u_{1s}^2) + g' \eta_s, \quad (8)$$

where $g' = g(\rho_2 - \rho_1)/\rho_0$ is the reduced gravity, ρ_0 is a reference density, and ρ_1 and ρ_2 are the upper and lower layer densities, respectively.

The character of the flow is determined by the composite Froude number at the sill (e.g., Baines 1995; Armi 1986), which with our notation can be written as

$$G_s^2 = \frac{u_{1s}^2}{g'(H_1 - \eta_s)} + \frac{u_{2s}^2}{g'(H_2 - d + \eta_s)}. \quad (9)$$

As long as G_s^2 is less than unity, the flow is symmetric over the sill, and the sill will just give rise to a local dent in the interface needed to accelerate the lower layer

over the sill (Fig. 2a). There will be no upstream or downstream influence of the sill, and therefore in order to calculate the interface elevation and layer velocities at the sill, (4) to (8) can be closed by setting $\eta_u = q_{bc} = 0$.

When the barotropic flow is increased such that

$$G_s^2 = 1. \quad (10)$$

The flow has the possibility to develop an asymmetric state over the sill (Fig. 2b; e.g., Baines 1995). If the flow is increased above the limiting case, the flow will develop an asymmetric state, and in order to maintain that state, the composite Froude number must remain equal to unity. The velocities and interface elevation at the sill will adjust to meet that requirement, which will change the volume fluxes and the upstream interface elevation such that $\eta_u \neq 0$ and $q_{bc} \neq 0$. With three extra variables η_u , q_{bc} , and G_s and two equations (9) and (10), an additional relation is required to close the system of equations. That relation is obtained from the far-field flow, which, as described below, is a radiation condition for long interfacial waves.

In the asymmetric state, the flow will develop a jump that adjusts to the downstream state. Energy is not conserved past the jump, but we assume that volume fluxes in each layer are conserved. In reality, mixing will increase the volume of intermediate water between the two layers, but we do not take this into account in the present approach. The baroclinic volume flux will therefore also be present downstream and cause radiation of interfacial waves in that direction.

b. Far-field flow

As long as the barotropic velocity is small enough for the composite Froude number to be less than unity at the sill, the far field does not feel the presence of the sill. When the flow becomes controlled at the sill, the changed volume fluxes in each layer cause baroclinic responses that propagate upstream and downstream from the sill. The approach we follow here is to let the barotropic flow increase with small increments. For each increment, the flow adjusts by radiating small internal waves on the baroclinic flow that exists at that moment, that is, due to the previously radiated internal waves. The dispersion relation for long internal waves in a two-layer flow with nonzero velocities u_1 and u_2 in the layers can be written as

$$\frac{(u_1 - c)^2}{g'h_1} + \frac{(u_2 - c)^2}{g'h_2} = 1, \quad (11)$$

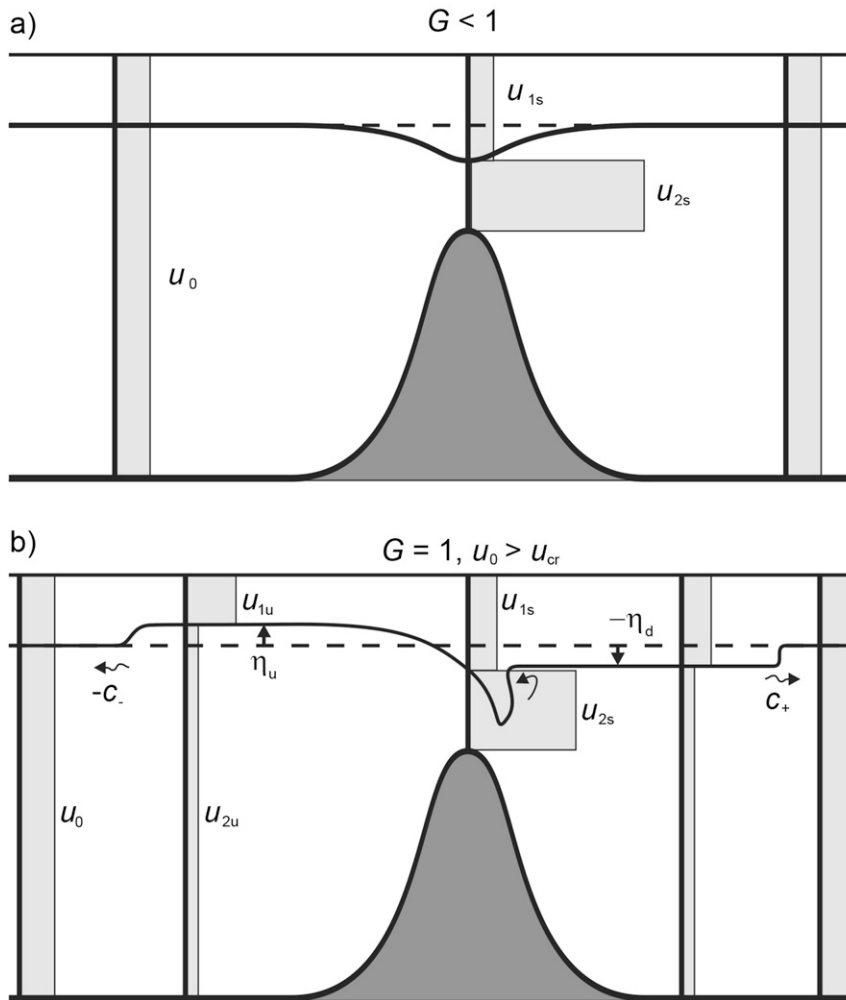


FIG. 2. Principal sketch of the flow situations (a) when the flow over the sill is subcritical and (b) when it is critical at the sill.

where $h_1 = H_1 - \eta$, and $h_2 = H_2 + \eta$ (see Fig. 2). One sees that the composite Froude number condition (9) emerges for zero phase velocity $c = 0$. The phase velocities can be found by solving the quadratic equation, yielding

$$c_{\pm} = U_m \pm \sqrt{c_0^2 - \frac{h_1 h_2}{H^2} (u_1 - u_2)^2} \quad (12)$$

(e.g., Armi 1986), where c_0 is the phase speed for the case of zero layer velocities ($u_1 = u_2 = 0$), c_+ and c_- correspond to the solution with + and -, respectively, and U_m is an advective current relative to which the internal waves move equally fast upstream and downstream:

$$U_m = \frac{u_1 h_2 + u_2 h_1}{H}. \quad (13)$$

Note that this is different from the barotropic current and is weighted toward the velocity in the thinnest layer.

If we consider an infinitesimal interface elevation change $d\eta$ with corresponding changes in layer velocities du_1 and du_2 propagating in the positive x direction with speed c , volume conservation gives us the following relations:

$$(u_1 - c)h_1 = (u_1 + du_1 - c)(h_1 - d\eta), \quad \text{and} \quad (14)$$

$$(u_2 - c)h_2 = (u_2 + du_2 - c)(h_2 + d\eta), \quad (15)$$

where we have neglected surface elevation changes according to the rigid-lid approximation. The derivatives of the layer velocities with respect to the interface elevation can therefore be written as

$$\frac{du_1}{d\eta} = -\frac{1}{h_1} (c - u_1), \quad \text{and} \quad (16)$$

$$\frac{du_2}{d\eta} = \frac{1}{h_2} (c - u_2). \quad (17)$$

From (14) and (15), the following exact relation can also be derived

$$\frac{dq_{bc}}{d\eta} = -c, \quad (18)$$

where, as in (4) and (5), q_{bc} is the baroclinic volume flux counted positive in the upper layer and negative in the lower layer. We now have a closed set of equations.

After the composite Froude number has reached unity at the sill, the procedure we consider is to stepwise increase the barotropic forcing beyond this point by

- calculating the upstream ($c_- < 0$) internal wave phase speed from (12), provided it exists;
- solving the equation system (4)–(10), with (18) providing the extra equation relating the increase in η_u and q_{bc} ;
- calculating the downstream internal wave phase speed from (12);
- solving for the downstream change in interface elevation using (18) with the now known change in baroclinic volume flux;
- calculating the changes in downstream layer velocities u_{1d} and u_{2d} from (16) and (17); and
- updating all layer velocities and interface elevations.

The solution of the nonlinear equation system is determined by the MATLAB routine `fsolve`, which works well for small increases in the barotropic velocity. The situation with a too strong barotropic forcing to provide an upstream wave, that is, $c_- \geq 0$, corresponds to upstream critical and supercritical conditions, and we assume that the interface elevation and baroclinic volume flux remain unchanged for stronger barotropic currents. This corresponds to flow types E and F in Baines (1984). We do not expect that this regime is properly represented by our model but leave it like this for future improvements.

c. Radiated energy fluxes and local dissipation

In the theoretical model as well as when analyzing the results of the numerical model, the energy balance is obtained for a control volume with vertical boundaries well upstream and downstream of the sill and the hydraulic jump but close to the sill in terms of an internal wavelength. When we look at a complete tidal cycle, each of these boundaries will go through being both upstream and downstream, so we now change our notation from upstream and downstream to left and right.

The mechanical energy equation can be written as [e.g., Gill 1982, his (4.7.3)]

$$\frac{\partial}{\partial t} \left[\frac{1}{2} \rho \mathbf{u}^2 + \rho g(z + H_1) \right] + \nabla \cdot \left\{ \left[\frac{1}{2} \rho \mathbf{u}^2 + \rho g(z + H_1) + p \right] \mathbf{u} \right\} = -\varepsilon, \quad (19)$$

where the second term is the potential energy relative to the mean interface positions, p is the pressure, ε is the dissipation of mechanical energy, and $\mathbf{u} = (u, w)$ is the velocity vector. There are additional viscous and diffusive fluxes, which we have neglected here. Integration over the control volume and averaging over a tidal cycle yields

$$\frac{\partial}{\partial t} \int_V \left[\frac{1}{2} \rho \mathbf{u}^2 + \rho g(z + H_1) \right] dV + F_R - F_L = - \int_V \bar{\varepsilon} dV, \quad (20)$$

where

$$F_{L(R)} = \left\{ \int_{-H}^0 \left[\frac{1}{2} \rho u^2 + \rho g(z + H_1) + p \right] u dz \right\}_{x=x_{L(R)}} \quad (21)$$

is the total energy flux through the left (right) boundary of the control volume, and the overbar denotes averaging over a tidal cycle. The second and third terms within the brackets of (21) contain large terms that almost balance, so we introduce perturbation variables as $\rho' = \rho - \bar{\rho}$, $p' = p - \bar{p}$, and $u' = u - \bar{u}$. In the following, we leave out left and right to simplify. Equation (21) can now be rewritten as

$$F = \int_{-H}^0 \overline{\left[\frac{1}{2} \rho u'^2 + \rho' g(z + H_1) + p' \right] u' dz} + \int_{-H}^0 \left[\frac{1}{2} \rho_0 (\bar{u}^2 + \overline{3u'^2}) + \bar{\rho} g(z + H_1) + \bar{p} \right] \bar{u} dz. \quad (22)$$

In the end, we are interested in the divergence of this flux over the sill, so purely symmetric terms with respect to the sill could be left out. In the second integral, the terms within square brackets can be expected to be symmetric, but the mean velocity (caused, e.g., by interfacial Stokes drifts and conversion of water masses due to mixing on the sill) turns out to be asymmetric, meaning that the whole term becomes asymmetric, representing a mean advection of kinetic and mean potential energies. The first two terms of the first integral represent the advection of perturbation kinetic and potential energies by the time-dependent part of the flow. The last term is the work performed by the perturbation pressure and is the dominating term in the limit of small perturbations and zero mean flow.

In the following, we assume that the second integral in (22), that is, the advection of potential and kinetic

energies by the mean flow, is negligible. In reality this means that the divergence of these mean advection terms become part of the dissipation term calculated below. In that case the energy flux can be written as

$$F \approx \int_{-H}^0 \overline{\left(\frac{1}{2}\rho u^2 + M'\right) u'} dz, \quad (23)$$

where $M' = \rho'g(z + H_1) + p'$ is the perturbation of the Montgomery potential. The energy flux can be separated into barotropic and baroclinic parts:

$$F_{BT} = \overline{M'_{BT} u'_{BT} H}, \quad F_{BC} = \int_{-H}^0 \overline{\left(\frac{1}{2}\rho u'^2_{BC} + M'_{BC}\right) u'_{BC}} dz, \quad (24)$$

where the barotropic and baroclinic parts of the Montgomery potential and velocity are defined as

$$M'_{BT} = \frac{1}{H} \int_{-H}^0 M' dz, \quad u'_{BT} = \frac{1}{H} \int_{-H}^0 u' dz, \quad (25)$$

and $M'_{BC} = M' - M'_{BT}$ and $u'_{BC} = u' - u'_{BT}$. In (24), we have not included the barotropic kinetic energy advection term because that term is symmetric with respect to the sill and does not contribute to the flux divergence.

We now, again, examine the integrated mechanical energy equation for the control volume [(20)]. Under periodic tidal forcing, and a small sill area compared with the total domain, the rates of change of mean energies within the volume are negligible. The energy input to the system comes from the barotropic tide interacting with the sill and should therefore be equal to the convergence C of barotropic energy at the sill, that is,

$$C = -\Delta F_{BT} \approx \Delta F_{BC} + \int \rho \varepsilon dV, \quad (26)$$

where $\Delta F = F_R - F_L$. In other words, the energy loss from the barotropic tides at the sill goes into the radiation of internal waves and local dissipation to heat within the volume.

Alternatively, the loss of barotropic energy can be calculated from the work done by the horizontal drag force at the sill on the barotropic flow. Neglecting friction, this can be calculated as the product of the barotropic velocity u_0 and the horizontal component of the pressure force on the bottom, that is,

$$C = -u_0 \int p[x, -H(x), t] \frac{dH}{dx} dx. \quad (27)$$

This can be seen, for example, by considering an analogy with the work needed to force a sill back and forth in a

quiescent fluid. As we will show below, the two ways to calculate the conversion of energy from model results give close to identical results.

In the theoretical model, the total energy loss in the upper layer is assumed to be zero, that is,

$$\frac{1}{2}u'^2_{1u} + \frac{M'_{1u}}{\rho_1} = \frac{1}{2}u'^2_{1d} + \frac{M'_{1d}}{\rho_1}. \quad (28)$$

Here, subscripts u and d denote the conditions just upstream of the sill and just downstream of the hydraulic jump, respectively (Fig. 2). An energy loss mainly in the lower layer is supported by observations of hydraulic flow over Stonewall bank on the Oregon shelf (Nash and Moum 2001) and is also the case for the type of hydraulic jumps investigated by Holland et al. (2002). In analogy with a one-layer hydraulic jump, it seems reasonable that it mainly is the active, supercritical layer that loses energy.

Without loss of generality, one can set $M'_{1u} = 0$, whereby (28) provides an equation to determine M'_{1d} . Under the hydrostatic approximation, the oscillating part of the lower-layer Montgomery potentials are related to those in the upper layer through

$$M'_2 = M'_1 + \rho_0 g' \eta. \quad (29)$$

So, when the far-field velocities and interface elevations have been determined as described above, the barotropic and baroclinic components of the velocities and Montgomery potentials can be extracted, and the energy fluxes F_{BC} and F_{BT} can be calculated according to (24). The local energy loss at the sill can be calculated from the lower-layer volume flux times the instantaneous decrease in lower-layer energy from the upstream to the downstream side of the sill, that is,

$$D = \int \rho \varepsilon dV = \rho h_{2u} u_{2u} \left(\frac{1}{2}u'^2_{2u} + \frac{M'_{2u}}{\rho_0} - \frac{1}{2}u'^2_{2d} - \frac{M'_{2d}}{\rho_0} \right). \quad (30)$$

This provides an alternative means of determining the radiation of baroclinic energy, since the sum of the local and radiated energy losses must be equal to the total energy loss from the barotropic tides, that is,

$$\Delta F_{BC} = -\Delta F_{BT} - \bar{D}. \quad (31)$$

The theory predicts a nonlinear response to the barotropic forcing, that is, with zero response at small velocities and rapidly increasing response after a certain threshold. This means that the radiated field is not sinusoidal. However, as will be seen below, the modeling results tend to yield a more sinusoidal response, with the

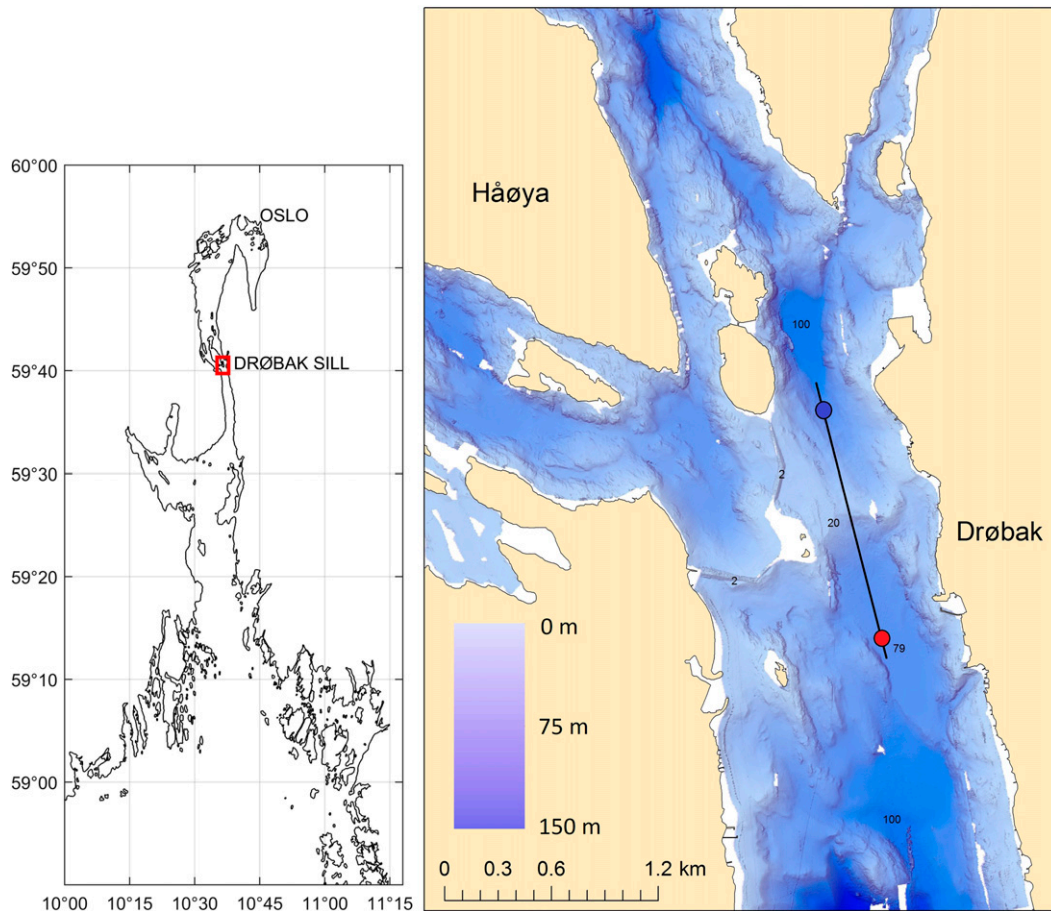


FIG. 3. Map of Oslo Fjord and the Drøbak sill with the black line showing the location of the transect in Fig. 4, and the blue and red circles showing the positions of the CTD casts in Fig. 4c.

amplitudes corresponding well to the predictions of the theory. This leads us to calculate the mean values in (31) based on the response at maximum tide, assuming a sinusoidal response to the sinusoidal forcing.

3. Dataset

The tides over the Drøbak sill (Fig. 3) were investigated during 3 days of June 2011 with 13 along-fjord and 2 cross-fjord, high-resolution transects of stratification and turbulence microstructure. The dataset is described in more detail in SALB. The Drøbak sill is about 18-m deep and separates basins of 80–100-m depth. During the experiment there was a rather strong halocline at about 11-m depth, and the barotropic tidal velocities were about 0.4 m s^{-1} over the sill. During some of the tidal periods we found strong hydraulic jumps during flood tide and none during ebb. We also found the opposite situation with jumps only during ebb and none during flood. SALB attribute these varying conditions to the presence of low-frequency baroclinic currents. Here, we will concentrate

on one of the tidal periods with weak mean baroclinic flows, corresponding to transects 9, 11, and 12 on 22 June (SALB). When comparing these observations with two-layer theory, a density difference of 12 kg m^{-3} between the two layers is representative for the real stratification. In SALB, the volume-integrated dissipation rates near the sill were estimated from dissipation rate estimates from microstructure transects by multiplying each observation-based value with a representative volume, taking into account the fjord width at that position and depth as well as the distance between casts.

4. Modeling study

The nonhydrostatic version of the MITgcm model (Marshall et al. 1997) was set up in two dimensions to study two-layer stratified flow over a sill. The model domain was 100 or 50 m deep rising to 30-m depth at the sill. The sill was described as

$$h(x) = H - de^{-(x\sigma/L)^2}, \quad (32)$$

TABLE 1. Summary of numerical cases; α is the thermal expansion coefficient. The em dash (—) signifies the same value as above.

Case name	U_0 (m s ⁻¹)	$\alpha \times 10^4$ (K ⁻¹)	H_1 (m)	H (m)	d (m)	$g' \times 1000$ (m s ⁻²)	U_s/c_0	$H_1/(H - d)$	d/H	$U_s/(\omega L)$
case_α10e-4_18	0.05	10	10.4	100	70	9.8	0.55	0.35	0.7	1.15
case_α10e-4_28	—	—	15.2	—	—	—	0.47	0.51	—	—
case_α10e-4_38	—	—	19.6	—	—	—	0.42	0.65	—	—
case_α10e-4_51	—	—	25.1	—	—	—	0.39	0.84	—	—
case_α10e-4_63	—	—	30.5	—	—	—	0.37	1.02	—	—
case_α1e-4_38	—	1	19.6	—	—	0.98	1.34	0.65	—	—
case_α2e-4_38	—	2	—	—	—	1.96	0.95	—	—	—
case_α5e-4_38	—	5	—	—	—	4.9	0.60	—	—	—
case_α100e-4_38	—	100	—	—	—	98	0.13	—	—	—
case_α40e-4_38	0.1	40	—	—	—	39.2	0.42	—	—	2.3
case_α160e-4_38	0.2	160	—	—	—	157	0.42	—	—	4.6
case_α2e-4_18	0.05	2	10.4	—	—	1.96	1.23	0.35	—	1.15
case_α2e-4_63	—	—	30.5	—	—	—	0.82	1.02	—	—
case_α20e-4_18	—	20	10.4	—	—	19.6	0.39	0.35	—	—
case_α20e-4_63	—	—	30.5	—	—	—	0.26	1.02	—	—
case_α10e-4_18sh	0.1	10	10.4	50	20	9.8	0.59	0.35	0.4	—
case_α10e-4_38sh	—	—	19.6	—	—	—	0.49	0.65	—	—
case_α10e-4_63sh	—	—	30.5	—	—	—	0.49	1.02	—	—

where $x = 0$ at the sill, L (=25 km) is half the domain width, and σ (=150) is a scaling variable giving a sill width of 235 m at the inflection point. The vertical grid resolution was 0.4 m at 20-m depth increasing to 1.2 m at the bottom. The horizontal grid resolution was 0.7 m near the sill, increasing toward 70 m at the lateral boundaries situated at $x = \pm 25$ km. The lateral boundaries were forced with a sinusoidal barotropic current with a period of 12 h. This is slightly different than the 12.4 h of the dominant M₂ tides of the observations, which does not influence the relevance of the results. The initial stratification was a two-layer stratification, with case-to-case varying strength and depth of the density step, as given in Table 1. The density was represented by temperature only, with a 1°C temperature difference between the layers and a thermal expansion coefficient α that varied between the cases. The temperature was kept equal to that at $t = 0$ at the lateral boundaries. Barotropic and baroclinic waves are reflected at the boundaries, so in order to avoid barotropic seiches, a gentle startup was applied to the lateral boundary conditions at the beginning, with an adjustment time scale of 1.5 h. Since the main emphasis of this study is the region near the sill, simulations were ended when reflected internal waves reached within the vicinity of the sill.

Energy fluxes were calculated at $x = \pm 1000$ m for a tidal cycle starting at 6 and ending at 18 h from the initiation of each simulation.

5. Results

Here, we first show some examples of the observations from SALB and compare with the predictions from the theory. Then we present some examples of the model

results with qualitative comparisons with the observations. Finally, we do quantitative comparisons between model and theory for a range of cases with varying tidal forcing and interface position relative to sill depth.

a. Observations versus theory

An example of a transect across the sill during flood tide with dissipation rates of turbulent kinetic energy and density stratification is shown in Fig. 4. The stratification is seen to be nearly two layer with the pycnocline situated at about 10-m depth and isopycnals situated somewhat higher in the water column upstream than downstream. The isopycnals on the upstream side, above about 40-m depth and below the pycnocline, bend up over the sill and dive down with the pycnocline on the downstream side before they jump up again, one by one, to meet the downstream levels. The dissipation rates are extremely high, above 10⁻³ W kg⁻¹ in the downstream region where the isopycnals jump up. For a more thorough discussion of these features, see SALB.

In Fig. 5, we show a comparison between the observed density field and the predicted two-layer, near-field response for the flood tide presented above and the following slack and ebb tides. During slack tide the theory predicts subcritical conditions over the sill, but during flood and ebb, the theory predicts a controlled situation at the sill with $G = 1$ and upstream- and downstream-propagating waves leaving an asymmetric situation at the sill. The two branches on the downstream side correspond to the supercritical branch prior to the jump and the downstream, subcritical situation left by the radiated wave of depression. The 19 kg m⁻³ isoline is seen to follow the theory rather well for all three cases both on

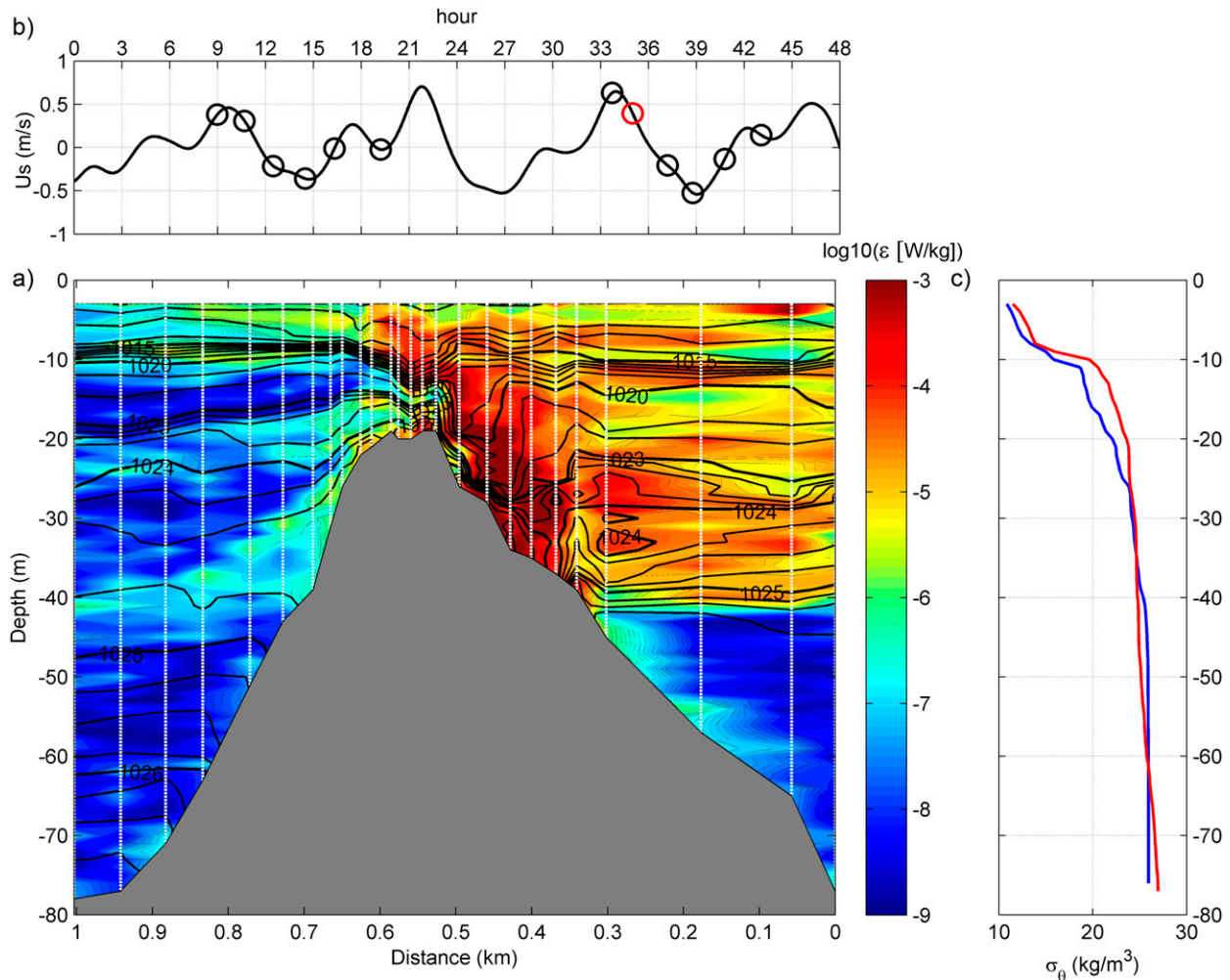


FIG. 4. (a) Transect 9 from south to north along the line shown in Fig. 3b, showing the dissipation rates (W kg^{-1} ; log10 scale) and density stratification (contours, kg m^{-3}) as functions of distance and depth. (b) Time series of the barotropic velocity over the sill (m s^{-1}) and the timing of all transects, with the actual transect in red. (c) The density profiles at the southern (red) and northern (blue) limits of the transect are given in the right-hand panel.

the upstream and downstream sides and near the sill, except during ebb, when the theory shows a slightly larger upstream response than the observations. Just downstream of the sill, the isoline is seen to follow the supercritical branch for some time before it jumps up toward the subcritical branch.

The volume-integrated local dissipation within 500 m from the sill crest was estimated from the observed dissipation rates (SALB) to be 1760 ± 640 , 45 ± 11 , and 1520 ± 570 kW for the flood, slack, and ebb transects shown in Fig. 5. The corresponding theoretical values are 800, 0, and 1580 kW, respectively, based on a channel width of 500 m. The differences between observational and theoretical estimates for the flood tide may be caused by the many assumptions in the theoretical estimates as well as by an underestimate in SALB of the

many uncertainties involved in estimating the integral of a very heterogeneous field from a rather coarse transect. However, the theoretical estimates are in the right order of magnitude, and especially for the ebb tide the correspondence is surprisingly good.

The theoretical estimate of the fraction of barotropic energy loss dissipated in the hydraulic jump is 75% for a barotropic velocity amplitude of $U_0 = 0.4 \text{ m s}^{-1}$. This is well within the band 60%–90% reported in SALB.

b. Numerical model results

Figure 6 shows an example of modeled temperature and velocity fields near the sill during flood tide. The numerical model results show a bottom layer that dives down on the downstream side of the sill and jumps up again in a rather chaotic manner farther downstream. The

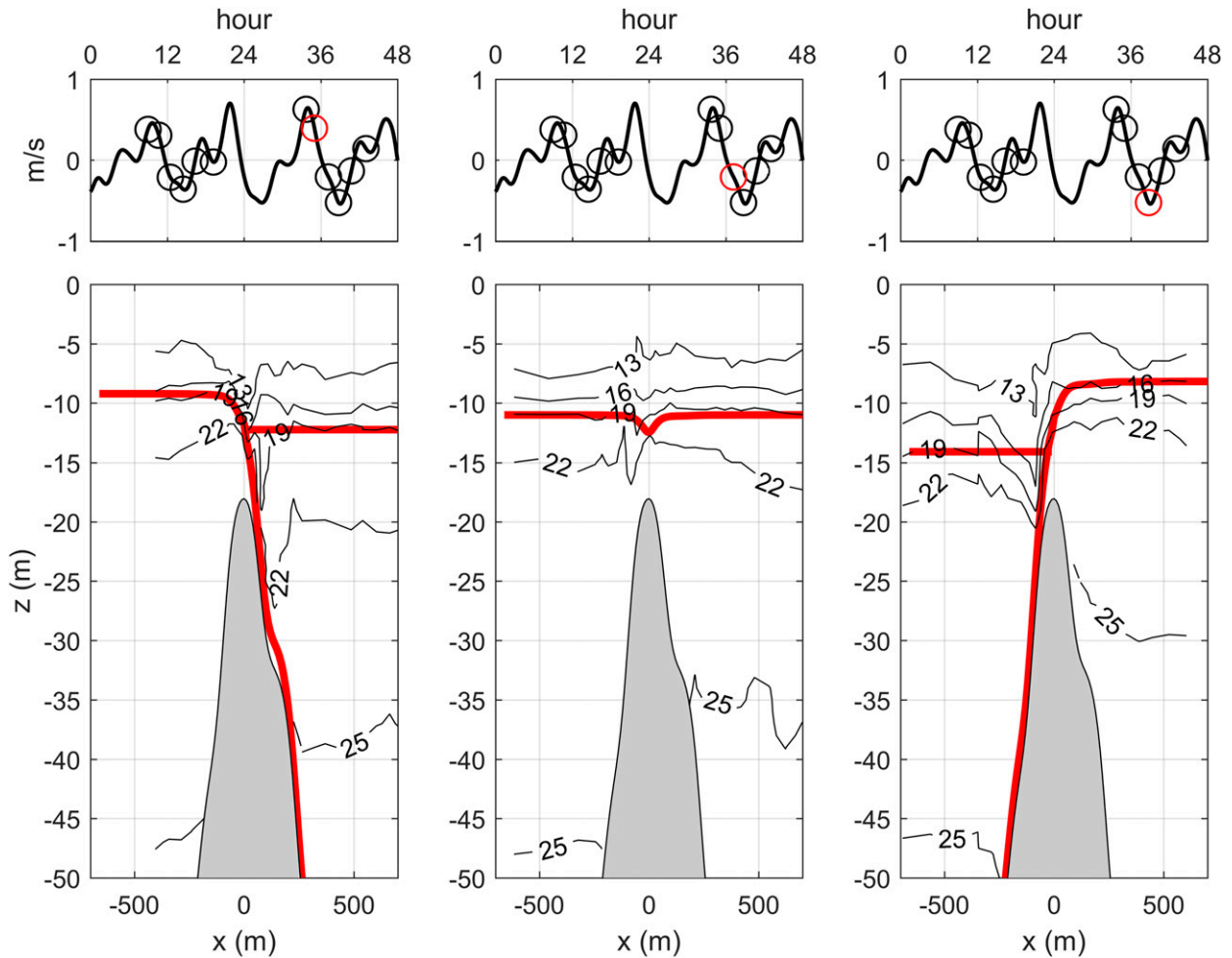


FIG. 5. (bottom) Transects over the sill with density anomaly contours and two-layer theory predictions of the interface positions (red lines). The lower red line on the downstream sides of the left- and right-hand panels corresponds to the supercritical branch the flow would take without a dissipative jump. (top) The barotropic tidal velocity over the sill and the timing of each transect (red circles).

model is also seen to resolve Kelvin–Helmholtz-like billows at the upper edge of the supercritical bottom current in the region where the observations show maximum dissipation rates. Eddies of upper-layer water are engulfed into the bottom layer more than 20 m below the interface before they seemingly disintegrate. A similar engulfment does not take place in the upper layer. This process therefore entrains more surface layer water into the bottom layer than opposite, that is, creating intermediary water masses downstream with properties closer to the bottom layer than to the upper layer. This mechanism is difficult to validate with observations, but the large dissipation rates observed quite deep along the downstream side of the sill (Fig. 3) indicate that turbulence and mixing is stronger below the pycnocline than above, as expected for this kind of mixing.

The velocity field shows a countercurrent in the layer of mixed water above the bottom jet. This

interfacial layer moves upstream when the tide slackens and transports mixed water to the other side of the sill in an internal, high-mode bore (not shown). Farther downstream, the bottom jet separates from the bottom and continues as an internal jet on top of a countercurrent at the bottom. This feature has been observed by, for example, Inall et al. (2004) in Loch Etive. The large shear between the jet and the stagnant water below in a water mass practically without stratification must cause large turbulence production and mixing.

c. Numerical model versus theory

To compare the model response with the theoretical predictions, the upper-layer thickness is estimated as

$$h_1 = \frac{1}{\Delta\rho} \int_{-H}^0 (\rho_{\max} - \rho) dz, \quad (33)$$

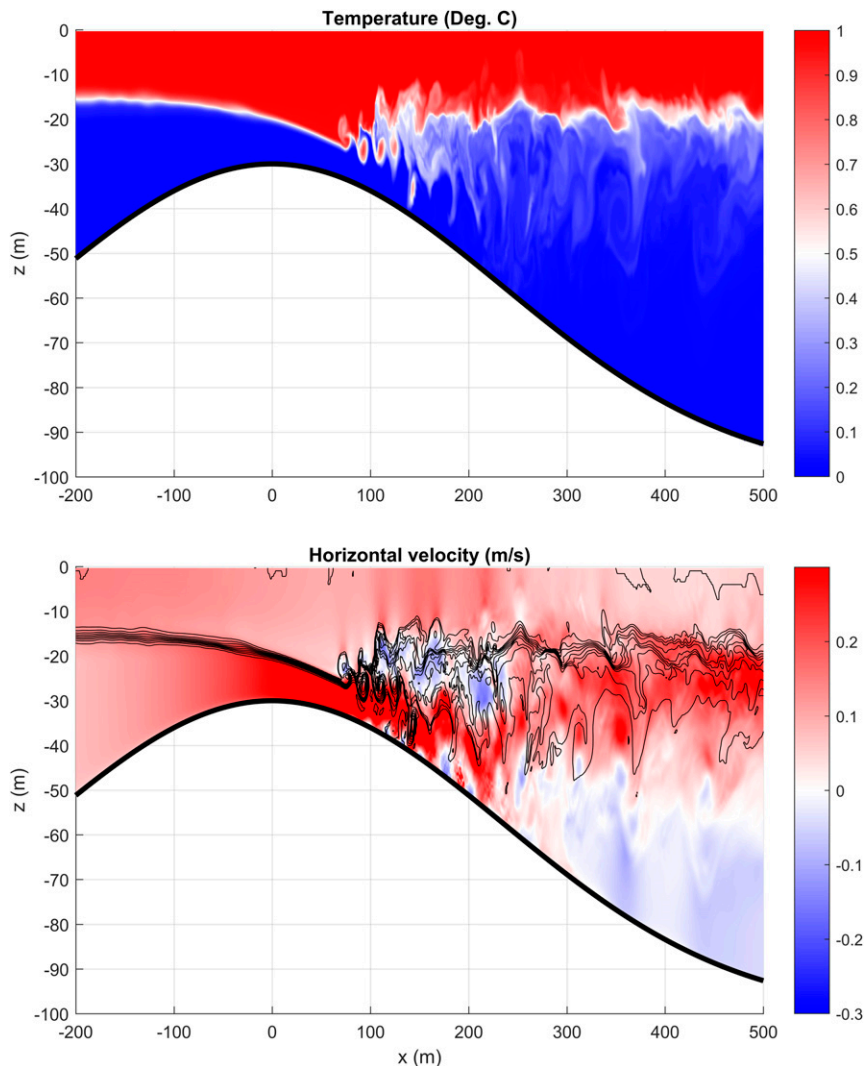


FIG. 6. Example of (top) modeled temperature and (bottom) horizontal velocity fields near the sill at flood tide. In the bottom panel temperature contours are shown with 0.1°C intervals.

where ρ_{\max} is the initial bottom layer density, and $\Delta\rho$ is the initial density difference. The model layer velocities are calculated as the average velocities in each layer. Figure 7 shows an example of the modeled and predicted interface positions and layer velocities on the sill and at the right-hand side of the sill (far-field solution) as functions of the barotropic velocity far from the sill. This is an example where the flow becomes critical at the sill but remains subcritical upstream. The interface positions have been made nondimensional with the upper-layer depth, and the velocities have been made nondimensional with the internal wave velocity c_0 in undisturbed water far from the sill. The model and theory tend to give similar results for all variables at the end points of the curves, but the theoretical prediction of zero baroclinic response for small velocities is not

reflected in the model that tends to respond more linearly to the forcing. The numerical model shows some high-frequency variability, as could be expected based on the short-wave variability seen in Fig. 6. However, the overall resemblance between model and theory is satisfactory.

When increasing the barotropic amplitude (Fig. 8), the theoretical solution reaches a situation when the upstream flow becomes supercritical and internal waves are swept downstream. The model and theory still give similar magnitudes in response, but the high-frequency variability in the numerical model output, especially in interface position, is much larger, and there is a hysteresis in the responses not accounted for in the theory. Inspection of the flow fields show that the high-frequency response is caused by large-amplitude internal wave

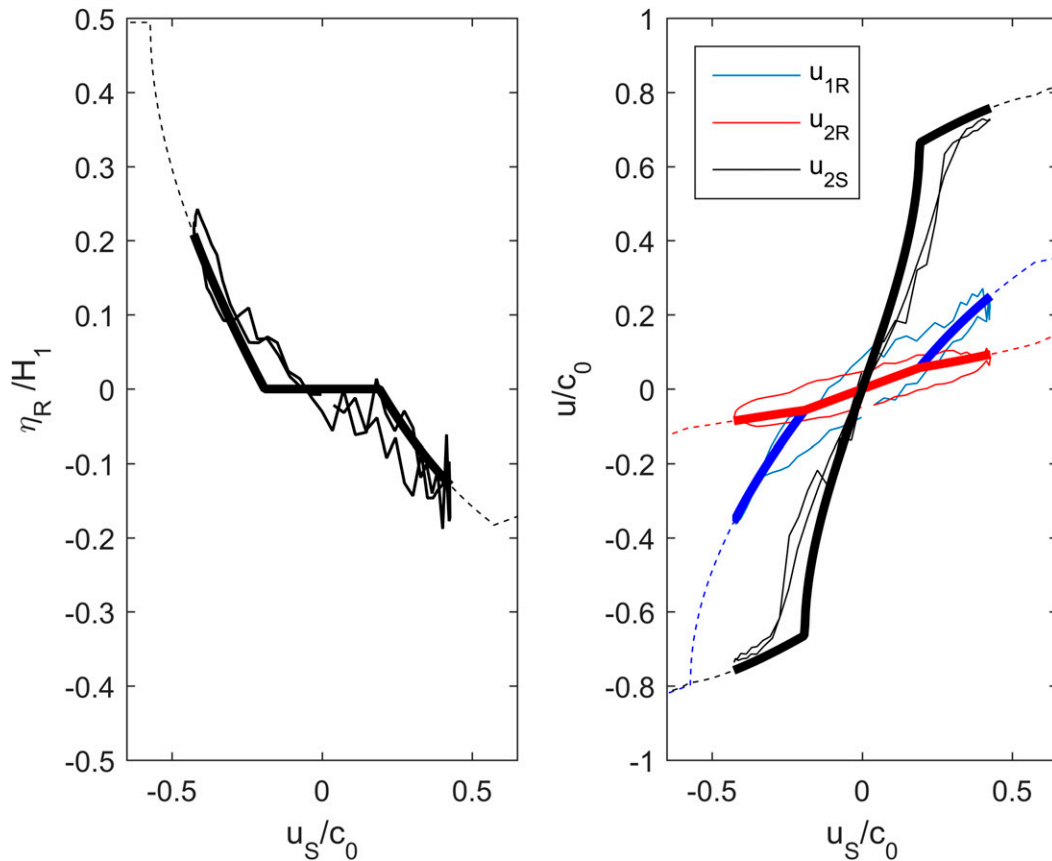


FIG. 7. Theoretical (thick) and modeled (left) interface positions and (right) layer velocities as function of barotropic velocity over one tidal cycle. The dashed lines show the theoretical prediction at larger barotropic velocities. The interface position is the far-field response to the right of the sill. The layer velocities are the lower-layer velocities at the sill (black) and to the right of the sill (red) and the upper-layer velocity to the right of the sill (blue). The results are for $U_s/c_0 = 0.43$ and $H_1/(H - d) = 0.65$.

trains that develop when the internal control is swept downstream and are propagating back over the sill when the tide slackens.

The barotropic energy loss predicted by model and theory is shown as function of barotropic velocity over the sill in Fig. 9a. The energy loss is made non-dimensional with the theoretical linear theory solution for internal wave generation with an interface situated at sill level (e.g., Stigebrandt and Aure 1989):

$$F_{\text{ref}} = \rho_0 \frac{d(H - d)}{H} U_s^2 c_0, \quad (34)$$

Note that this is twice the value used in, for example, Stigebrandt and Aure (1989), who only consider wave radiation on one side of the sill. The model and theoretical predictions generally agree well, except at small velocities for interfaces above sill level, where the model gives small energy losses even for cases where the theory does not, and for large velocities, where the theory also tends to give smaller values than the model.

For the interface situated at sill level (black line), the predictions tend toward the reference value for small barotropic velocities [(34)], as expected. The model and theoretical results show the same general decrease with increasing height of the interface above sill level. The bends in the theoretical curves occur when the flow becomes supercritical upstream. The purest wave radiation cases, where we expect the theory to work best, are therefore situated to the left of these bends. The barotropic energy losses calculated from the bottom drag [27] are also shown and are seen to give almost identical results to those calculated from barotropic wave radiation.

The radiation of baroclinic energy (Fig. 9b) also show a general agreement between model and theory, and the curves show a similar behavior as the barotropic energy losses (Fig. 9a), except that these are somewhat smaller because part of the barotropic energy is lost locally and does not radiate away. The energy that does not radiate away is shown in Fig. 9c. This part is seen to

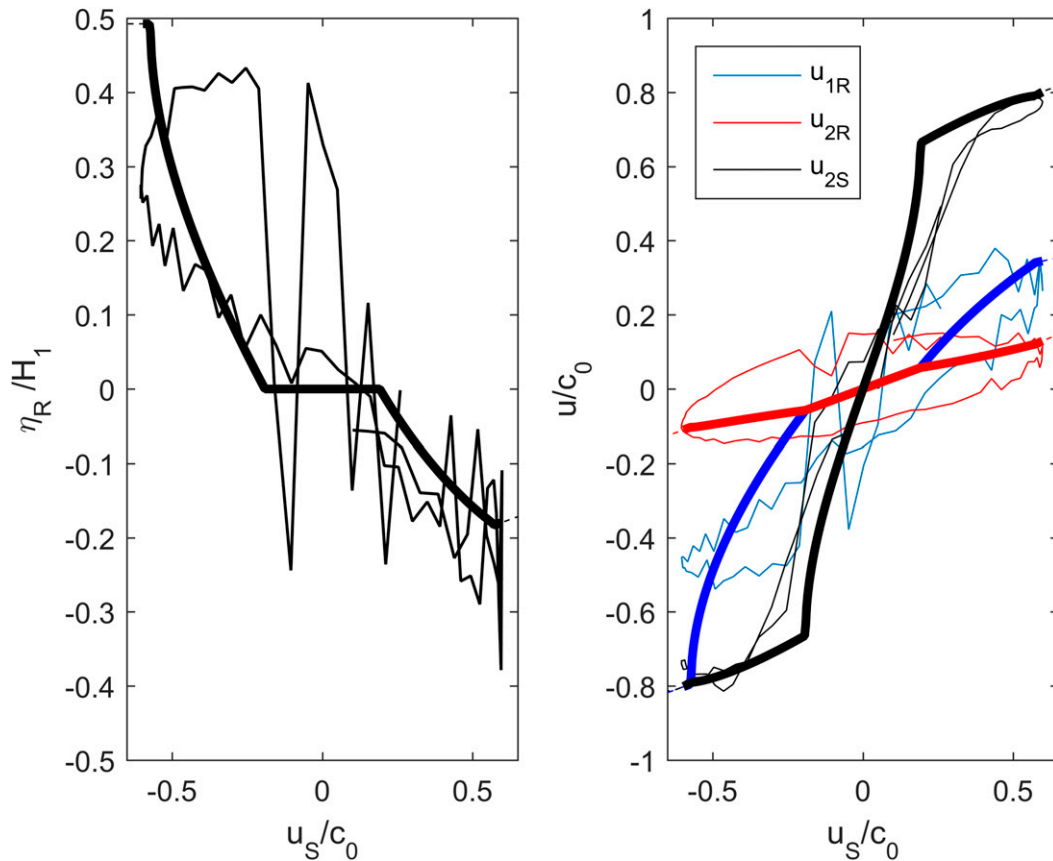


FIG. 8. As in Fig. 7, but for a case with $U_s/c_0 = 0.6$.

be about 20% for the interface positioned at sill level and for weak forcing (Fig. 9d), increasing toward 100% for the interface approaching the surface. Also for increasing velocities, the radiative part of the barotropic energy loss decreases, as one would expect when waves are not allowed to radiate upstream from the sill.

To test the theory for a different relative sill height, the model was run for three cases with a sill with height of 40% of the basin depth rather than 70%, as in the above examples. The theoretical predictions and the model results for these three cases are shown in Fig. 10. Generally the nondimensional curves look much like those for the taller sill, but there is a tendency that the baroclinic radiation constitutes a smaller fraction of the barotropic energy loss for the smaller sill. The agreement between model and theory is as good as for the taller sill.

Finally, one of the main assumptions of the theory is that the excursion length over the sill is large compared to the sill width [(3)]. We have run the numerical model with nondimensional excursion lengths of $U_s/(\omega L) = 1.1, 2.3,$ and 4.6 (Table 1), and the results of these runs give next to identical nondimensional energy fluxes

(Fig. 9), so the requirement of (3) can probably safely be relaxed to $U_s/(\omega L) > 1$.

6. Discussion

The magnitude and partitioning of barotropic energy loss estimated from high-resolution observations over a real fjord sill have been investigated with a theoretical model and with a fully nonlinear numerical model with idealized geometry and stratification. Both theory and model describe the observed interface responses on each side of the sill, the total energy loss from the barotropic tides, and the partitioning of this energy between radiated baroclinic energy and local energy loss in a satisfactory manner. When running the model on a range of different nondimensional forcing strengths and interface positions, the model results and theory also compare favorably, except in the weak and strong ends of the forcing regime, where the model generally tends to give larger barotropic energy losses than the theory.

The fact that the theory compares relatively well with results from the much more complicated numerical model (Figs. 9, 10) indicates that many of the

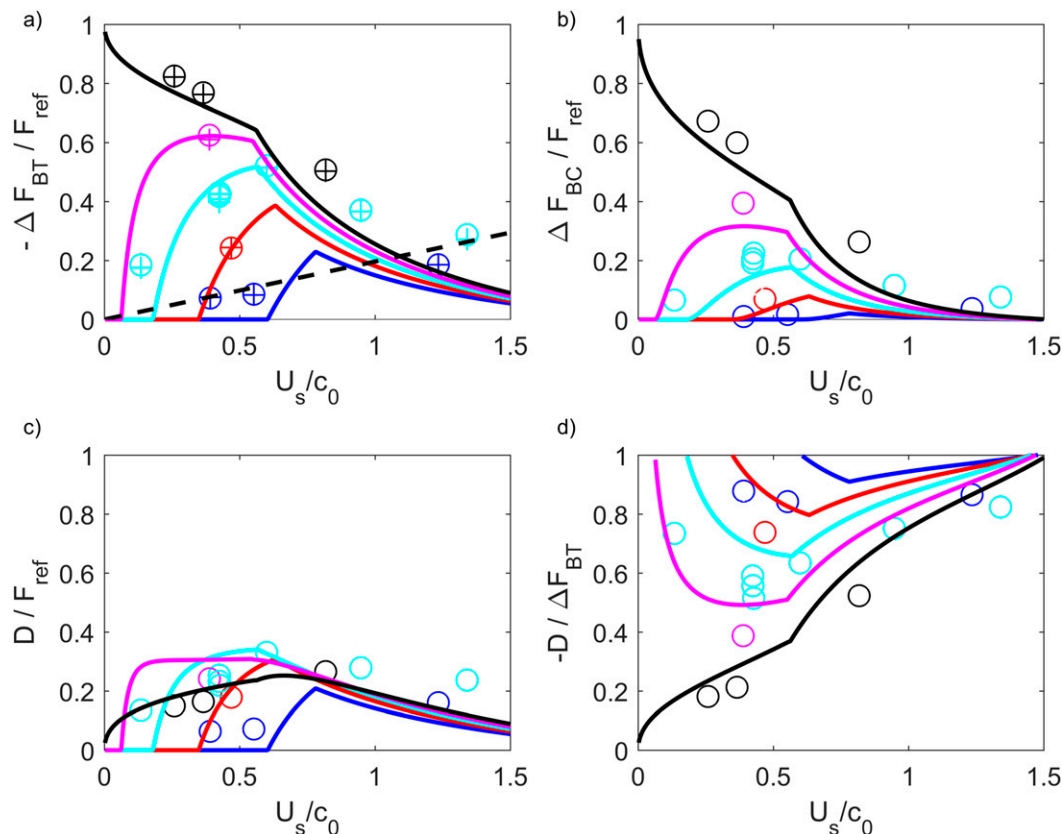


FIG. 9. The (a) loss of barotropic energy, (b) radiation of baroclinic energy, (c) rate of local dissipation, and (d) fraction of barotropic energy dissipated locally at the sill as function of the nondimensional barotropic velocity over the sill for sill height $d/H = 0.7$. The lines correspond to theory, and the circles correspond to model results. The barotropic energy loss estimated from the bottom drag [(27)] is also shown (+). The various colors correspond to upper-layer depths, $H_1/(H - d)$ equal to 1 (black), 0.83 (magenta), 0.67 (cyan), 0.5 (red), and 0.33 (blue). The black dashed line in (a) shows the theoretical prediction for a jet at the sill [see (35)].

assumptions of the theory are reasonable. The most questionable assumption is that the mixing in the downstream hydraulic jump does not strongly influence the layer volume fluxes. Note that this assumption does not influence the hydraulic control or the upstream wave propagation, only the local energy loss and the downstream-propagating wave. As an opposite extreme, one could assume that the entrainment into the lower layer is as strong as the lower-layer blocking at the sill, that is, that the lower-layer downstream volume flux is equal to the lower-layer barotropic volume flux. That would cause a density change in the lower layer close to the sill and a baroclinic adjustment of the resulting lower-layer horizontal density gradient. However, the blocking effect on the downstream interface would be cancelled, and there would be no downstream-propagating interfacial waves. In the present theory, the upstream- and downstream-propagating waves contribute with about equal amounts of energy flux, so in that case the

internal wave radiation would be about half of that predicted in the present theory. Figures 9b and 10b clearly show that the present assumption, with a small tendency to underestimate the radiation, fits much better with the numerical model results than a theory with half that estimate. We therefore interpret these results as a confirmation that mixing does not impose a strong influence on the radiated energy, the total energy loss, and the partitioning between radiated and locally lost energy. A somewhat provocative, but promising, implication of this is that both the local dissipation and radiated energy is governed by large-scale hydraulic processes that can be predicted by theory and models that do not necessarily have to include the small-scale processes causing the energy loss and mixing.

This does not mean that mixing does not influence the dynamics. Mixing does influence the dynamics by generating mixed fluid of intermediary density that moves away from the sill. That is a subtidal baroclinic motion

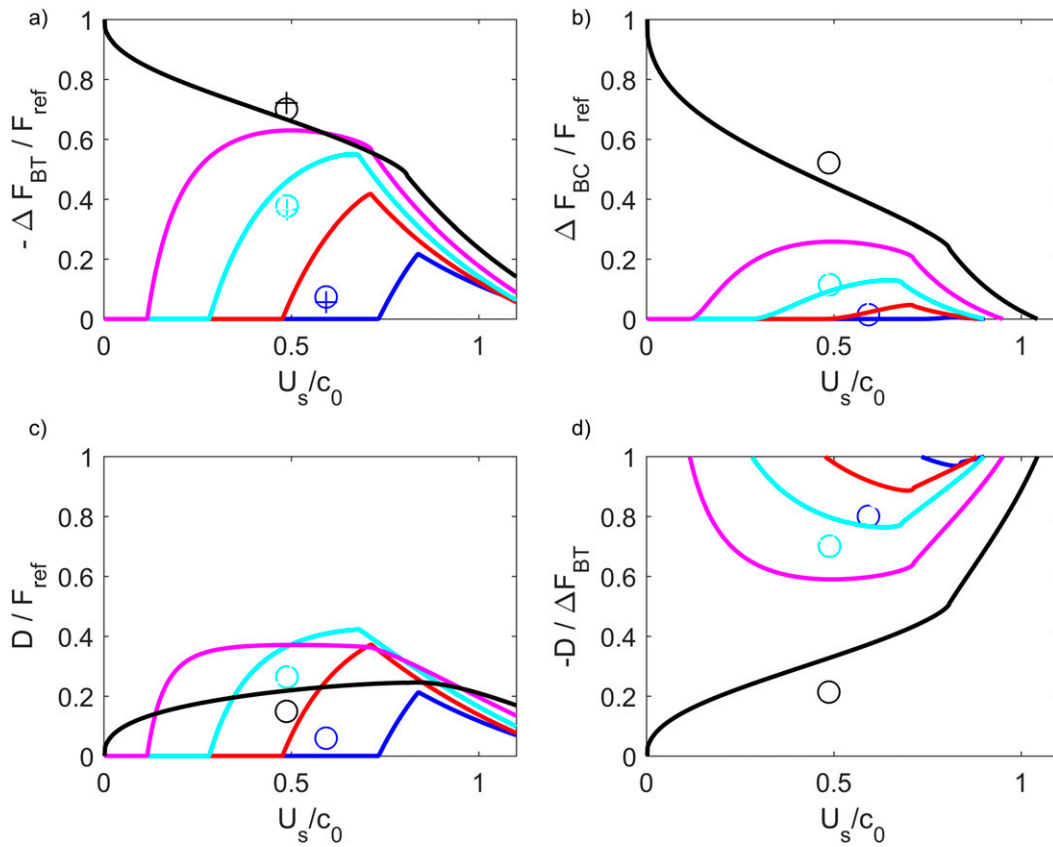


FIG. 10. As in Fig. 9, but for sill height $d/H = 0.4$.

that goes on during all tidal phases and is clearly seen in animations of the model results (not shown) and in the right-hand side of the bottom panel of Fig. 6.

The results of the theoretical and numerical investigations (Figs. 9, 10) show that the barotropic energy loss for a two-layer fluid compares best with the linear theory reference estimate [(34)] for small-amplitude motions ($U_s/c_0 \rightarrow 0$) when the interface is situated at sill level, as is also assumed in that theory. The results also show that the barotropic energy loss decreases relative to this reference case, when the interface height rises above sill level and when the barotropic forcing increases. The ratio of local energy loss to barotropic energy loss is smallest, about 20%, for an interface situated at sill level and increases toward 100% as the interface rises toward the surface. The main reason for this increase in local energy loss and decrease in radiated energy is that the blocking effect of the sill becomes much weaker when the interface is far above the sill. It is this effect that explains why so large a fraction of the barotropic tidal energy loss at the Oslo Fjord sill is lost locally. It does not, however, explain why as much as two-thirds of the tidal energy loss is radiated from the Knight Inlet sill, where the interface is situated at about

10–20-m depth, far above the sill at about 60 m. According to the present theory less than 10% should be allowed to escape the sill in that case (blue line in Fig. 9b). One possible explanation for this discrepancy may be the two-layer approximation that neglects deeper stratification and higher modes. The downstream response in Knight Inlet clearly is not a first-mode response (e.g., Farmer and Armi 1999).

The theory does not allow for higher vertical-mode responses at the sill, and it remains a question how this influences the results. The observations suggest that higher modes are present in the real fjord (Fig. 4), since the layers below 40-m depth do seem to be more or less blocked by the sill. This is seen by the isopycnals below this level not rising toward the sill by the low dissipation rates below this level as well as by the line of increased dissipation rates starting at 40-m depth upstream and rising toward the sill, as an indication of shear at this level. That is, in reality the water below 40 m is not advected over the sill, whereas in a two-layer model there is no vertical shear in the lower layer. However, the numerical model does to some degree allow higher modes as the stratification develops from the initial two-layer stratification toward a more continuous stratification, and we do

not see any strong change in the results when analyzing the initial tidal period as compared to the later periods. This indicates that the higher modes do not influence the overall results when the lower-layer stratification is weak. We suggest that the higher modes mainly influence the results in the region with weak forcing where the two-layer theory predicts zero response but where higher modes could possibly be generated. This effect could be investigated by including a second interface in the theory and model and/or by introducing a linear stratification below the interface in the model, which we leave for future research. It may possibly be this mechanism that gives the relatively high radiation from the Knight Inlet sill.

The model was tested with three values of the non-dimensional excursion length [(3)], all giving similar results. This shows that the theoretical assumption of hydraulic, quasi-steady flow at the sill is realistic for the investigated cases, but it does not provide a lower bound for the forcing or sill widths where this is not the case. The fact that the lower-layer velocity is typically much larger than the barotropic velocity over the sill probably makes (3) a rather conservative assumption.

Stigebrandt and Aure (1989) suggest an alternative barotropic energy loss mechanism at large velocities ($U_s > c_0$) in so-called jet fjords where the barotropic kinetic energy over the sill is assumed to be lost in a jet inside the sill:

$$F_{\text{jet}} = \frac{0.42}{2} \rho_0 (H - d) U_s^3. \quad (35)$$

This is shown as the black dashed line in Fig. 9a, which should be valid for large values of the barotropic forcing. There is no indication that the barotropic energy loss shows such an increasing trend at large velocities, neither in theory nor in model results, and this expression is seen to predict too large energy losses. It may be speculated that this is the reason why the predicted mixing efficiency (fraction of barotropic energy loss used to mix the basin water) of the fjord basins investigated in Stigebrandt and Aure (1989) is much lower for jet basins than for wave basins; basically, the real barotropic energy loss may be much smaller than predicted for these jet basins. It may, however, be noted that the present results are obtained for a pure 2D case, whereas real fjord mouths are often both narrow and shallow, for example, causing strong 3D jets, which are absent in 2D configurations.

Even though the present theory does not cover all flow types of stratified flow over topography, it does provide simple estimates of local dissipation and radiated energy due to tidal interaction with steep topography that may be expected to work well when there is a strong

pycnocline not too far above the topography. Such situations are common in fjords, archipelagos, and on the continental shelf. With some further steps, the theory can be developed into a parameterization of mixing over rough topography in coastal circulation models that are too coarse to represent the small-scale processes investigated in this work. This would provide an alternative to present parameterizations, using a constant fraction of the barotropic energy loss (e.g., Simmons et al. 2004), but also to the more advanced parameterization suggested by Klymak et al. (2010). An important difference between the parameterization of local dissipation in this model and that of Klymak et al. (2010) is that our dissipation tends to scale as the square of the tidal velocity (Fig. 9c), whereas that of Klymak et al. (2010) scales as the cube of the tidal velocity. The high-resolution, nonhydrostatic simulations of Musgrave et al. (2016) support dissipation rates that scale in the vicinity of the square of the tidal velocity.

Acknowledgments. The computations were performed on resources provided by the Swedish National Infrastructure for Computing (SNIC) at C3SE (Chalmers Centre for Computational Science and Engineering) computing resources. The work has been funded by the Norwegian Research Council (Project 184944) and by the Swedish Research Council (Grant 621-2008-2689).

REFERENCES

- Alford, M. H., and Coauthors, 2015: The formation and fate of internal waves in the South China Sea. *Nature*, **521**, 65–69, doi:10.1038/nature14399.
- Armi, L., 1986: The hydraulics of two flowing layers with different densities. *J. Fluid Mech.*, **163**, 27–58, doi:10.1017/S0022112086002197.
- Baines, P. G., 1984: A unified description of two layer flow over topography. *J. Fluid Mech.*, **146**, 127–167, doi:10.1017/S0022112084001798.
- , 1988: A general method for determining upstream effects in stratified flow of finite depth over long two-dimensional obstacles. *J. Fluid Mech.*, **188**, 1–22, doi:10.1017/S0022112088000618.
- , 1995: *Topographic Effects in Stratified Flows*. Cambridge University Press, 482 pp.
- Chu, V. H., and R. E. Baddour, 1977: Surges; waves and mixing in two-layer density stratified flow. *Proceedings of the 17th Congress of the International Association for Hydraulic Research*, Vol. 1, IAHR, 303–310.
- Egbert, G. D., and R. D. Ray, 2000: Significant dissipation of tidal energy in the deep ocean inferred from satellite altimeter data. *Nature*, **405**, 775–778, doi:10.1038/35015531.
- Farmer, D., and L. Armi, 1999: Stratified flow over topography: The role of small-scale entrainment and mixing in flow establishment. *Proc. Roy. Soc. London*, **A455**, 3221–3258, doi:10.1098/rspa.1999.0448.
- Gill, A. E., 1982: *Atmosphere–Ocean Dynamics*. Academic Press, 662 pp.

- Holland, D. M., R. R. Rosales, D. Stefanica, and E. G. Tabak, 2002: Internal hydraulic jumps and mixing in two-layer flows. *J. Fluid Mech.*, **470**, 63–83, doi:10.1017/S002211200200188X.
- Inall, M., F. Cottier, C. Griffiths, and T. Rippeth, 2004: Sill dynamics and energy transformation in a jet fjord. *Ocean Dyn.*, **54**, 307–314, doi:10.1007/s10236-003-0059-2.
- Klemp, J., R. Rotunno, and W. Skamarock, 1997: On the propagation of internal bores. *J. Fluid Mech.*, **331**, 81–106, doi:10.1017/S0022112096003710.
- Klymak, J. M., and M. C. Gregg, 2004: Tidally generated turbulence over the Knight Inlet sill. *J. Phys. Oceanogr.*, **34**, 1135–1151, doi:10.1175/1520-0485(2004)034<1135:TGTOTK>2.0.CO;2.
- , and Coauthors, 2006: An estimate of tidal energy lost to turbulence at the Hawaiian Ridge. *J. Phys. Oceanogr.*, **36**, 1148–1164, doi:10.1175/JPO2885.1.
- , S. Legg, and R. Pinkel, 2010: A simple parameterization of turbulent tidal mixing near supercritical topography. *J. Phys. Oceanogr.*, **40**, 2059–2074, doi:10.1175/2010JPO4396.1.
- Li, M., and P. Cummins, 1998: A note on hydraulic theory of internal bores. *Dyn. Atmos. Oceans*, **28**, 1–7, doi:10.1016/S0377-0265(98)00045-1.
- Marshall, J., A. Adcroft, C. Hill, L. Perelman, and C. Heisey, 1997: A finite-volume, incompressible Navier Stokes model for studies of the ocean on parallel computers. *J. Geophys. Res.*, **102**, 5753–5766, doi:10.1029/96JC02775.
- Munk, W., and C. Wunsch, 1998: Abyssal recipes II: Energetics of tidal and wind mixing. *Deep-Sea Res. I*, **45**, 1977–2010, doi:10.1016/S0967-0637(98)00070-3.
- Musgrave, R. C., J. A. MacKinnon, R. Pinkel, A. F. Waterhouse, and J. D. Nash, 2016: Tidally driven processes leading to near-field turbulence in a channel at the crest of the Mendocino Escarpment. *J. Phys. Oceanogr.*, **46**, 1137–1155, doi:10.1175/JPO-D-15-0021.1.
- Nash, J. D., and J. N. Moum, 2001: Internal hydraulic flows on the continental shelf: High drag states over a small bank. *J. Geophys. Res.*, **106**, 4593–4611, doi:10.1029/1999JC000183.
- Saenko, O. A., and W. J. Merryfield, 2005: On the effect of topographically enhanced mixing on the global ocean circulation. *J. Phys. Oceanogr.*, **35**, 826–834, doi:10.1175/JPO2722.1.
- Simmons, H. L., S. R. Jayne, L. C. S. Laurent, and A. J. Weaver, 2004: Tidally driven mixing in a numerical model of the ocean general circulation. *Ocean Modell.*, **6**, 245–263, doi:10.1016/S1463-5003(03)00011-8.
- Sjöberg, B., and A. Stigebrandt, 1992: Computations of the geographical distribution of the energy flux to mixing processes via internal tides and the associated vertical circulation in the ocean. *Deep-Sea Res.*, **39A**, 269–291, doi:10.1016/0198-0149(92)90109-7.
- Staalstrøm, A., L. Arneberg, B. Liljebladh, and G. Broström, 2015: Observations of turbulence caused by a combination of tides and mean baroclinic flow over a fjord sill. *J. Phys. Oceanogr.*, **45**, 355–368, doi:10.1175/JPO-D-13-0200.1.
- Stacey, M. W., 1985: Some aspects of the internal tide in Knight Inlet, British Columbia. *J. Phys. Oceanogr.*, **15**, 1652–1661, doi:10.1175/1520-0485(1985)015<1652:SAOTIT>2.0.CO;2.
- Stashchuk, N., M. Inall, and V. Vlasenko, 2007: Analysis of supercritical stratified tidal flow in a Scottish fjord. *J. Phys. Oceanogr.*, **37**, 1793–1810, doi:10.1175/JPO3087.1.
- Stigebrandt, A., 1976: Vertical diffusion driven by internal waves in a sill fjord. *J. Phys. Oceanogr.*, **6**, 486–495, doi:10.1175/1520-0485(1976)006<0486:VDDBIW>2.0.CO;2.
- , 1979: Observational evidence for vertical diffusion driven by internal waves of tidal origin in the Oslofjord. *J. Phys. Oceanogr.*, **9**, 435–441, doi:10.1175/1520-0485(1979)009<0435:OEFVDD>2.0.CO;2.
- , and J. Aure, 1989: Vertical mixing in basin waters of fjords. *J. Phys. Oceanogr.*, **19**, 917–926, doi:10.1175/1520-0485(1989)019<0917:VMIBWO>2.0.CO;2.
- , —, and J. Molvær, 1996: Oxygen budget methods to determine the vertical flux of particulate organic matter with application to the coastal waters off western Scandinavia. *Deep-Sea Res. II*, **43**, 7–21, doi:10.1016/0967-0645(95)00077-1.
- White, B. L., and K. R. Helfrich, 2014: A model for internal bores in continuous stratification. *J. Fluid Mech.*, **761**, 282–304, doi:10.1017/jfm.2014.599.
- Winters, K. B., and L. Armi, 2012: Hydraulic control of continuously stratified flow over an obstacle. *J. Fluid Mech.*, **700**, 502–513, doi:10.1017/jfm.2012.157.
- , and —, 2013: The response of a continuously stratified fluid to an oscillating flow past an obstacle. *J. Fluid Mech.*, **727**, 83–118, doi:10.1017/jfm.2013.247.
- Wood, I. R., and J. E. Simpson, 1984: Jumps in layered miscible fluids. *J. Fluid Mech.*, **140**, 329–342, doi:10.1017/S0022112084000628.